Capsular polysaccharide conformations in pneumococcal serotypes 19F and 19A.

Michelle Kuttel[a,*], Graham E. Jackson[b], Mpho Mafata[b], Neil Ravenscroft[b],

[a]*Department of Computer Science, University of Cape Town,Cape Town, South Africa*
[b]*Department of Chemistry, University of Cape Town,Cape Town, South Africa*

Abstract

Streptococcus pneumoniae is a significant pathogen in children. Although the PCV7 pneumococcal conjugate vaccine has reduced pneumococcal disease, non-vaccine serotype 19A infection has increased, despite expectations of cross-protection from vaccine serotype 19F. Serotype 19A is included in the new PCV13 vaccine, but not in PCV10.

In the solution simulations of 19F and 19A oligosaccharide chains reported here, both polysaccharides form unstructured random coils, with inflexible repeat units linked by mobile phosphodiester linkages. However, there are clear conformational differences. In the 19F repeat unit, the rhamnose residue is nearly orthogonal to the other residues, whereas 19A has residues in similar orientations. This finding is corroborated by key inter-residue distances calculated from NMR NOESY experiments. Further, 19F is predominantly in extended conformations, whereas 19A exhibits a high prevalence of tight hairpin bends.

These conformational differences may account for a lack of antibody cross-

*Tel:+27 21 6505107, email: mkuttel@cs.uct.ac.za

protection between serotypes 19F and 19A.

Keywords: Streptococcus pneumoniae, vaccine, pneumococcal, cross protection, Molecular Modelling

---

1. Introduction

The capsular polysaccharides of pneumococci are essential for bacterial virulence; vaccine-induced serum antibodies against capsular polysaccharides confer resistance to pneumococcal disease. Pneumococcal serogroup 19 is currently responsible for the bulk of pneumococcal disease. Within serogroup 19, which comprises serotypes 19F, 19A, 19B and 19C, disease is caused chiefly by 19A and 19F[1]:

→4)-β-D-Man*p*NAc-(1→4)-α-D-Glc*p*-**(1→2)**-α-L-Rha*p*-(1-P→

19F capsular polysaccharide

→4)-β-D-Man*p*NAc-(1→4)-α-D-Glc*p*-**(1→3)**-α-L-Rha*p*-(1-P→

19A capsular polysaccharide

While serotypes 19F and 19A have very similar trisaccharide repeating units, cross-protection for these serotypes has not been clearly demonstrated: the 7-valent Prevnar vaccine (PVC7) contains 19F, but does not appear to elicit clinically meaningful cross-protection against 19A invasive pneumococcal disease[2]. Indeed, despite current widespread vaccination with 19F in PCV7, the proportion of infections caused by serotype 19A has increased: currently, 19A appears to be the most prevalent and antibiotic-resistant pneumococcal serotype[3,4]. This apparent lack of cross-protection for 19F

and 19A is in agreement with early studies published for the pneumococcal polysaccharide vaccines: although the 19F polysaccharide vaccine raised cross-reactive antibodies against 19A, they displayed low functionality in the opsonophagocytic killing assay.[5] This assay is currently used as a surrogate assessment of the clinical efficacy of pneumococcal conjugate vaccines[6]; the opsonic ability of antibodies has been correlated to their avidity in pre-clinical studies[7]. These studies led to the inclusion of the serotype 19A polysaccharide in the second-generation 23-valent vaccine[8,9]. The higher valency conjugate vaccine PCV13, which aims to provide greater coverage of the emerging pneumococcal strains, also contains both serotypes 19F and 19A. Immunogenicity studies for PCV13 showed the presence of functional antibody activity predictive of protection against serotype 19A disease[10], which has been confirmed by recent post-licensure studies[11]. In contrast, while the PCV10 vaccine does not contain serotype 19A, indirect protection against 19A is claimed based on the conjugation chemistry employed in PCV10 for the serotype 19F-diphtheria toxoid vaccine component[12,13]. However, in our opinion, this is doubtful, as the random activation chemistry utilising cyanylation (PVC10) or periodate oxidation (PCV13) relies on levels of activation that are sufficient to permit conjugation, but low enough so as not to affect the structural integrity of the native polysaccharide antigen.

In this work, we continue our systematic investigation of the molecular basis of cross protection in pneumococcal serotypes 19F and 19A which we began with simulation of the conformation of the repeating units in the carbohydrate antigens[14]. This first study predicted a wider range of conformations for 19F than the more constrained 19A trisaccharide, suggesting a probable

conformational difference between the polysaccharides. Here we extend this investigation to solution simulations of 19F and 19A oligosaccharide chains comprising three- and six repeat units, as well as experimental NMR NOESY measurements on the 19F and 19A polysaccharides.

2. Experimental Section

We analyse the 19F and 19A pneumococcal polysaccharides according to the following glycosidic linkages and corresponding abbreviations.

Linkage	Abbreviation	Polysaccharide
β-D-Man*p*NAc-(1→4)-α-D-Glc*p*	M14G	19F and 19A
α-L-Rha*p*-(1-P→4)-β-D-Man*p*NAc	RP4M	19F and 19A
α-D-Glc*p*-**(1→2)**-α-L-Rha*p*	G12R	19F
α-D-Glc*p*-**(1→3)**-α-L-Rha*p*	G13R	19A

The two-bond (1→X) glycosidic linkages in M14G, G12R and G13R are defined by the torsion angles $\phi = H1'$–$C1'$–O–CX and $\psi = C1'$–O–CX–HX. These definitions for ϕ and ψ are analogous to ϕ_H and ψ_H in IUPAC convention. In the case of the RP4M phosphodiester linkage, the four dihedral angles are defined as $\phi = H1'$–$C1'$–O–P, $\psi = C1'$–O–P–O, $\omega = O$–P–O–$C4$ and $\epsilon = P$–O–$C4$–$H4$.

2.1. Molecular Dynamics Simulations

All simulations were performed with the NAMD molecular dynamics program[15] version 2.9 (employing NAMD CUDA extensions for calculation of long-range electrostatics and nonbonded forces on graphics processing

units[16]) and run on a 12 core, 4 TeslaM2090 GPU server with 64GB RAM per core and 6GB DDR5 per GPU.

Water was simulated with the TIP3P model[17]. Carbohydrates were modeled with the CHARMM36 additive force field for carbohydrates,[18,19] with ad hoc extensions for the phosphodiester linkage, as follows. Although parameters for phosphate substituents were recently added to the CHARMM carbohydrate force field[20], these do not yet extend to flexible anomeric phosphodiester linkages. Therefore, this work necessitated adjustments to the CHARMM carbohydrate force field to represent the β-D-Man*p*NAc residue, as well as the α(P$\rightarrow$4) glycosidic phosphodiester linkage for pyranose rings. In accordance with suggestions from the lead CHARMM force field developer, the ManNAc residue was adapted from the parameters in the existing βMan and αGlcNAc residues and bond, angle and dihedral parameters for the phosphodiester linkages were taken from similar linkages in the existing force field, or from the CHARMM nucleic acid force field where necessary[21].

Initial configurations of the three- and six repeating unit oligosaccharides (hereafter termed RU3 and RU6) for both 19F and 19A were built using our in-house software CarbBuilder[22], which employs the psfgen[23] tool to create "protein structure"(psf) files for modelling with a specified CHARMM force field and the NAMD molecular dynamics program. Using CarbBuilder, the glycosidic linkage dihedrals were set to initial values within the global energy minima previously identified[14]: ϕ,$\psi = 51°, -6°$ for the M14G linkage, ϕ,$\psi = -41°, -24°$ for the G12R linkage (19F) and ϕ,$\psi = -28°, 43°$ for the G13R linkage (19A). The phosphodiester linkage, α-L-Rha*p*-(1-P$\rightarrow$4)-β-D-Man*p*NAc, was set to $\phi, \psi, \omega, \epsilon = -50°, 180°, -180°, -180°$ to produce initial

extended structures.

These initial oligosaccharide structures were optimised through 1000 steps of standard NAMD minimization in vacuum and then solvated (using the *solvate* plugin to the Visual Molecular Dynamics (VMD)[24] analysis package) in a periodic cubic unit cell with randomly distributed sodium ions to electrostatically neutralize the system: the RU3 structures used a 60 × 60 × 60 Å cube and three sodium ions, while the RU6 structures used a 110 × 110 × 110 Å cube and six sodium ions.

The RU3 MD simulations ran for 150 ns and the larger, computationally expensive RU6 simulations for 100 ns. All MD simulations were preceded by a 30 000 step minimisation phase, with a temperature control and equilibration regime involving 10 K temperature reassignments from 10 K culminating in a maximum temperature of 300 K. Equations of motion were integrated using a Leap-Frog Verlet integrator with a step size of 1 fs and periodic boundary conditions. Simulations were performed under isothermal-isobaric (nPT) conditions at 300 K maintained using a Langevin piston barostat[25] and a Nose-Hoover[26,27] thermostat.

Long-range electrostatic interactions were treated using particle mesh Ewald (PME) summation, with $\kappa = 0.20$ Å^{-1} and PME grid dimensions of 60 for the RU3 systems and 110 for the RU6 systems. Non-bonded interactions were truncated with a switching function applied between 12.0 and 15.0 Å to groups with integer charge. The 1-4 interactions were not scaled, in accordance with the CHARMM force field recommendations.

Subsequent analysis of the simulations used time series frames 25 ps apart. Molecular conformations extracted from the MD simulations were depicted

with VMD, where necessary using the PaperChain visualization algorithm for carbohydrates[28] to highlight the glycan rings. For comparison with NMR measurements, average effective proton-proton distances, r, were calculated from the equilibrated RU3 simulations using the equation

$$r = < r_{i,j}^{-6} >^{-\frac{1}{6}} \tag{1}$$

where $r_{i,j}$ is the instantaneous atomic distance between atoms i and j. The radius of gyration, R_g, is a common measure of the conformation of a polymer and represents the root-mean-square distance of a collection of atoms from their common centre of mass. We calculated R_g with VMD using the carbon atoms in each oligosaccharide chain as:

$${R_g}^2 = \frac{1}{n}\sum_{i=1}^{n}(R_i - R_c)^2 \tag{2}$$

where R_c is the centre of mass, R_i the position of atom i and n the number of atoms. The squared end-to-end distances, d^2, were measured as

$$d^2 = (R_{C2} - R_{C4})^2 \tag{3}$$

where R_{C4} is the position of the carbon atom $C4$ on the first ManNAc residue and R_{C2} is the position of the carbon atom $C2$ (or $C3$ for the 19A oligosaccharide) on the rhamnose at the terminal reducing end.

Conformations from both RU3 trajectories were clustered using VMD's internal *measure cluster* command to calculate clusters according to the quality threshold algorithm.[29] Clustering was performed with a cut-off of 3.0 on an RMSD fit to the carbon, oxygen and phosphate atoms involved in the glycosidic linkages.

2.2. NMR

19F and 19A polysaccharide samples were obtained from PATH's pneumococcal vaccine project. The samples (10 mg) were dissolved in D_2O (0.6 mL, Aldrich) and transferred to 5 mm NMR tubes (Wilmad). NMR spectra were obtained using a Bruker Avance III 600 MHz NMR spectrometer equipped with a BBO Prodigy cryoprobe. The probe temperature was set at 303 K and the spectra were acquired and processed using standard Bruker software (Topspin 3.2). ^{1}H NMR spectra were referenced to the residual cell wall polysaccharide signal at 3.23 ppm. Two dimensional NMR spectra were collected in the phase sensitive mode, TOCSY (mixing time, 120 ms) and NOESY (mixing time, 250 ms) using presaturation to suppress the water resonance. Spectral assignments were based on literature assignments and confirmed by use of ^{1}H-^{1}H and ^{1}H-^{13}C correlation experiments[30,31]. Linearity of the NOE build-up curves was demonstrated using a series of 1D NOE experiments (mixing times ranging from 100 to 400 ms). Inter-proton distances were estimated from the integrated cross-peak intensities of key 2D NOESY peaks by the isolated spin pair approximation[32]:

$$r_{i,j} = r_{ref}\left(\frac{a_{ref}}{a_{ij}}\right)^{\frac{1}{6}} \tag{4}$$

where $r_{i,j}$ is the inter proton distance to be estimated and a_{ij} the corresponding cross-peak intensity. The ManNAc H1/ManNAc H3 distance calculated from the RU3 solution simulation (2.38 Å, an r^6 average) was used as a reference distance.

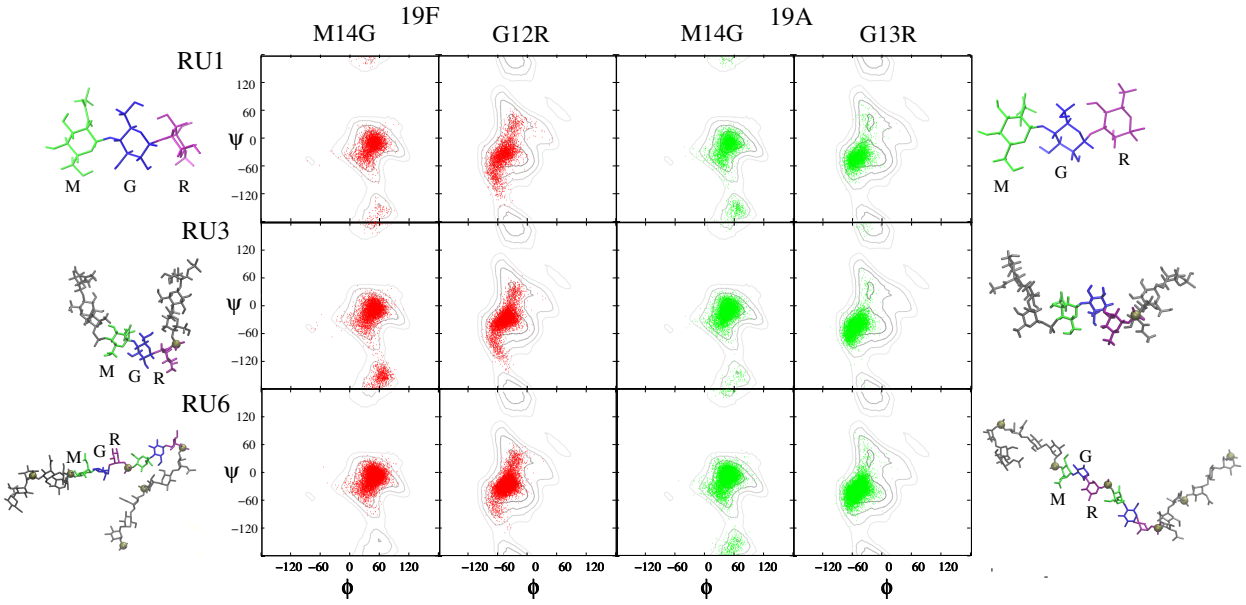

Figure 1:

3. Results and discussion

We begin our analysis of the pneumococcal capsular polysaccharides in serotypes 19F and 19A with investigation of the conformation and dynamics of the repeat unit and then progress to the preferred conformation and dynamics of the RU3 and RU6 polysaccharide chains.

3.1. Repeating unit conformation

The repeating units in the RU3 and RU6 polysaccharides remain relatively rigid in solution, as is clear from a comparison of the M14G and G12R/G13R dihedral angle time series for RU1 (prior work[14]), RU3 and RU6 simulations shown in Figure 1.

Comparison across the RU1, RU3 and RU6 simulations in Figure 1 reveals that additional RU do not affect the distribution of dihedral angle values sig-

nificantly. This indicates that, for both the 19F and the 19A polysaccharides, the RU1 simulations give a good indication of the dihedral angle distribution in the corresponding polymer. The mean ϕ, ψ values for the 19F G12R linkage in the RU3 simulations are ϕ, ψ = -45.63° (15.28), -30.50° (27.50), while for the 19A G13R linkage ϕ, ψ = -53.84° (13.30), -42° (26.50). However, the 19F repeating unit is more conformationally varied than the 19A repeating unit: while the 19A shows a normal distribution about the mean for both ϕ and ψ, 19F has two minor populations at $\psi > 0°$ ($\approx$ 10%) and $\psi < 90°$ ($\approx$ 10%). This is in accordance with our detailed analysis of the single repeating units in 19F and 19A, which showed two families of "bent" conformations for the G12R linkage, that are not apparent in the G13R linkage.[14]

In these comparatively rigid repeat units, across all simulations there is a marked difference in the relative orientation of the Rha residue in 19F as compared to 19A. In 19F, the orientation of the plane of Rha is nearly orthogonal to the Glc and ManNAc residues, whereas in 19A the planes of the sugar rings are all in roughly parallel orientations - compare representative conformations of 19F (Figure 2, left) and 19A (Figure 2 left) repeat units. A direct measure of this difference relative orientation of the Rha are the inter-residue H1 Glc/H1 Rha and H1 Glc/H3 Rha distances. Figure 2 shows a time series plot of these distances for the middle residue in the RU3 unit simulations of 19F (red) and 19A (green) (RU1 and RU6 simulations show the same distribution). 19F and 19A show distinct, separate populations for these distances (Figure 2, middle). The orthogonal arrangement of Rha in 19F brings the Glc H1 atom into close proximity with the Rha H1 atom, while stretching the H1 Glc/H3 Rha distance (representative structure with

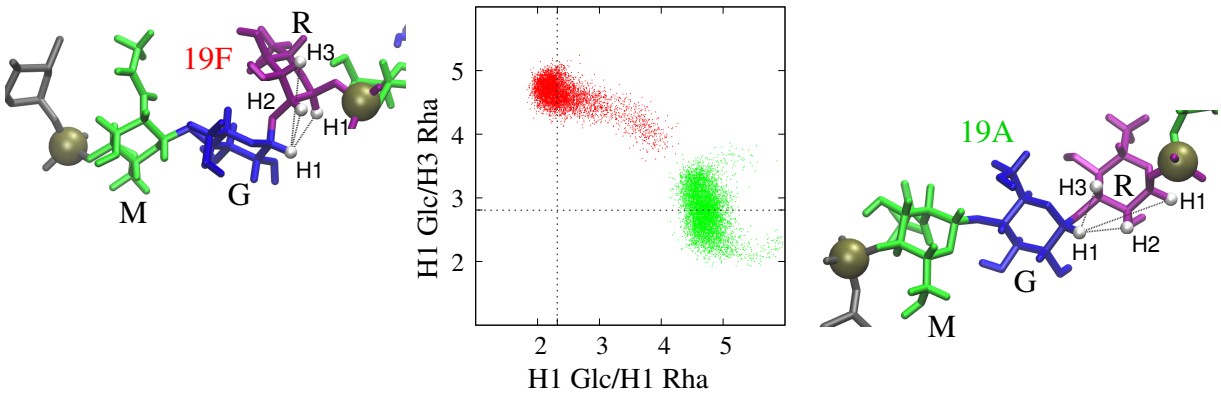

Figure 2:

Table 1:

	19F		19A	
Atomic distance (Å)	exp.	sim.	exp.	sim.
H1 Glc/H1 Rha	2.32	2.28	-	4.68
H1 Glc/H2 Rha	2.49	2.41	2.44	2.25
H1 Glc/H3 Rha	-	4.57	2.81	2.66
H1 ManNAc/H4 Glc	2.33	2.30	2.19	2.31

distances indicated shown in Figure 2, left). The opposite holds for 19A: Glc H1 is in close proximity to Rha H3, but relatively distant from Rha H1 (representative structure with distances indicated shown in Figure 2, right). In contrast, the Glc H1/Rha H2 distance is similar for both the 19F and 19A repeat units.

This finding is corroborated by our NMR NOESY experiments (Figure 3). The H1 Glc/H2 Rha peak is present in NOESY for both 19F and 19A (indicating close proximity of these atoms in the polysaccharides), but the H1 Glc/H3 Rha peak is absent in the 19F NOESY and the H1 Glc/H1 Rha

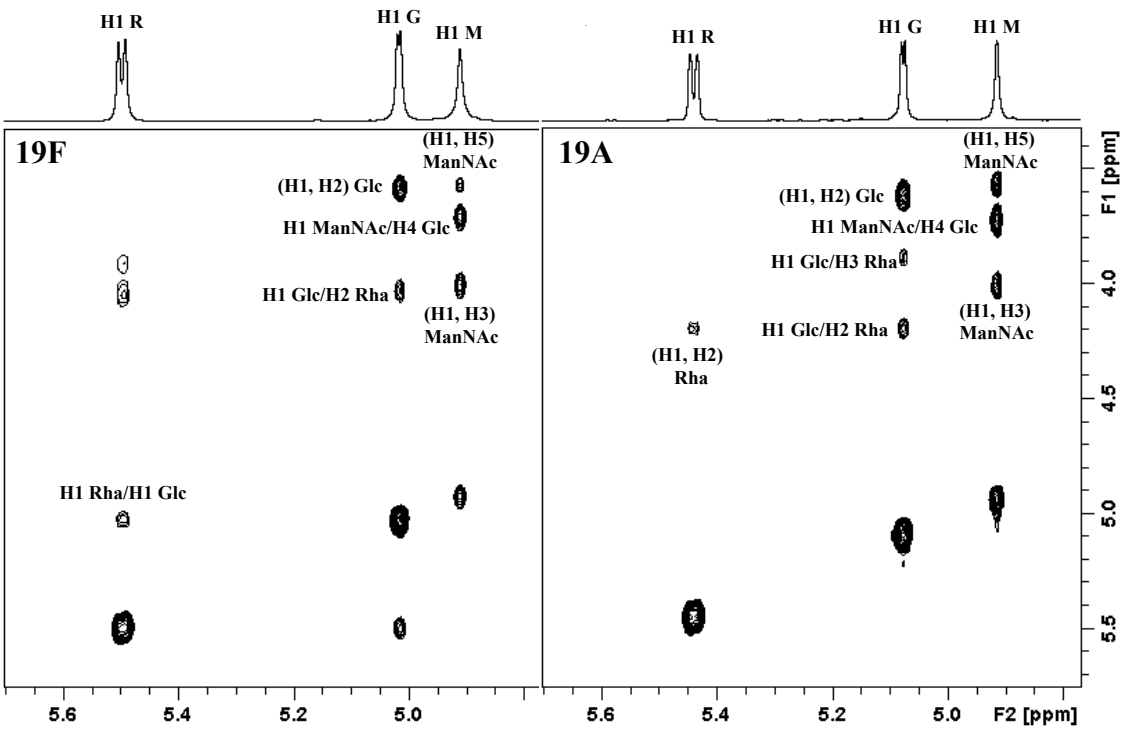
H1 R
H1 G
H1 M
19F
(H1, H5) ManNAc
(H1, H2) Glc
H1 ManNAc/H4 Glc
H1 Glc/H2 Rha
(H1, H3) ManNAc
H1 Rha/H1 Glc
H1 R
H1 G
H1 M
19A
(H1, H5) ManNAc
(H1, H2) Glc
H1 ManNAc/H4 Glc
H1 Glc/H3 Rha
(H1, H3) ManNAc
H1 Glc/H2 Rha
(H1, H2) Rha
F1 [ppm]
F2 [ppm]

Figure 3:

peak is absent in the 19A NOESY. Further, the distances calculated by peak integration (Table 1) show good agreement between simulation and NMR.

3.2. Polymer hydrodynamics

Although the repeat units are relatively rigid, in our simulations, the three repeat unit (RU3) oligomers for 19F and 19A polymers are very mobile - a consequence of the very flexible phosphodiester linkage. In both 19F and 19A, the peripheral ϕ and ϵ torsions for the phosphodiester linkage are constrained to conformations in the range $-60°$ to $+50°$. Rotations about the phosphodiester linkage are therefore primarily determined by the central phosphodiester linkage dihedrals: ψ and ω. These C-O-P-O dihedrals each have three principal minimum energy conformations: $-85°, 85°$ and $175°$. Although transitions between these minima occur frequently through the simulations, both 19A and 19F favour the $\psi, \omega = -85°, -85°$ conformation, which causes a bend in the phosphodiester bond. However, 19F shows an increased population of the secondary minimum conformation $\psi, \omega = 85°, 85°$ which is associated with extension of the phosphodiester linkage.

The RU3 simulations demonstrate that the 19F and 19A R are mobile, disorganised molecules that form random coils, with no well-defined tertiary structure. There is a wide variation in R_g for both the 19F and 19A molecules (Figure 4i), which alternate between extended and compact conformations throughout the 150 ns of simulation time. However, the RU3 simulations show a difference in average R_g (indicated by the dashed lines in the graph Figure 4i): after discarding the first 10 ns as equilibration, 19F has $< R_g >$=10.43(1.12) Å, while 19A has $< R_g >$=9.07(1.37) Å. As a further comparison, for the same period the 19F RU3 oligomer shows a mean

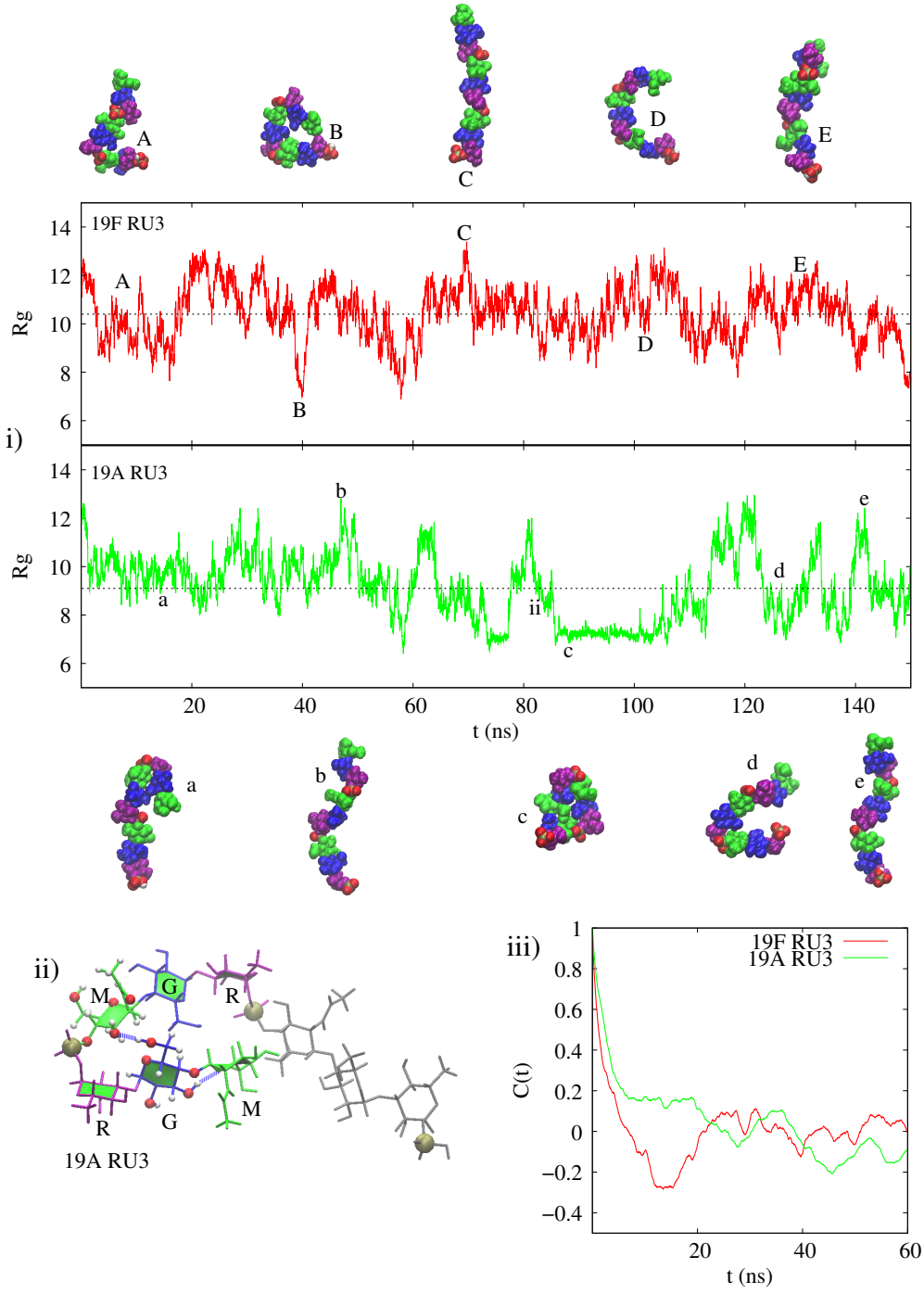
A
B
C
D
E
i)
19F RU3
Rg
t (ns)
19A RU3
a
b
c
d
e
ii
ii)
M
G
R
19A RU3
iii)
19F RU3
19A RU3
C(t)
t (ns)

Figure 4:

squared end-to-end distance of 823 Å^2, while 19A has 474 Å^2. 19F has a higher frequency of extended structures (Figure 4i, conformations C and E), 19A more persistent compact structures (Figure 4i, conformations c and d). This behaviour is a direct consequence of the different repeat unit conformations for 19F and 19A, as follows. The parallel arrangement of residues in 19A allows for close stacking of residues in successive RU's in tight hairpin bends about the phosphodiester linkage (e.g. Figure 4i conformation a). This allows for strong shifting network of Glc-Glc' or Glc-ManNAc' hydrogen bonds, an example of which is shown in Figure 4ii, where an Glc HO6 - ManNAc' O2 hydrogen bond is formed across the bend. These interactions maintain the hairpin bend for up to 20 ns (e.g. conformation c in Figure 4i). Indeed, our clustering analysis reveals that the 19A RU3 strand is in a hairpin bend conformation about one of the two internal phosphodiester linkages for approximately 75% of simulation time. In contrast, while hairpin bends do occur for 19F (e.g. conformation B in Figure 4i), they do not bring successive RUs into as close enough proximity for hydrogen bonding and are therefore comparatively short-lived: the 19F RU3 strand is in hairpin bend conformations for only 6% of the simulation, while very extended conformations (e.g. conformation C in Figure 4i) occur for 25% of the simulation time.

The autocorrelations of R_g for the RU3 strands indicate relative long decay times of $\approx$ 5-10 ns (Figure 4iii), with 19A having the longer decay. These extended decay times are a result of entanglements promoted by self-interactions between methyl, hydroxymethyl and N-acetyl groups on neighbouring repeating units in both 19F and 19A. The longer decay for 19A is a

consequence of the close residue stacking that facilitates hairpin bends. This propensity for self-entanglements has the consequence that, after 100 ns of simulation time, the computationally expensive simulations of RU6 of 19F and 19A cannot be said to have reached equilibrium with regards to chain conformation, as is evident from the R_g time series for these molecules (Figure 5i). However, it is also clear that the hydrodynamic behaviour of the longer RU6 strands is consistent with the corresponding RU3 simulations, with constant interconversions between compact and extended structures (compare structures A-E and a-e in Figure 5i). Also, although the simulations have not equilibrated, the 19F simulation shows R_g values associated with more extended structures, whereas the trend of the 19A simulation is towards more compact conformations. Once more, long-lived hairpin bends are prevalent for the 19A oligosaccharide: Figure 5iii shows an example hairpin conformation, with Glc-Glc' and ManNAc'-Glc hydrogen bonds stabilizing the bend.

4. Conclusions

Although polymer dynamics in our simulations of the 19F and 19A provides evidence of very mobile random chains for both molecules, this is a consequence of the very flexible phosphodiester linkage: both the 19F and 19A repeating units are relatively rigid. Most significant, there is a marked difference in the repeating unit conformation of 19F and 19A, with 19F having Rha oriented nearly orthogonal to the Glc and ManNAc residues, whereas 19A has the planes of the sugar rings in parallel orientations. This finding is corroborated by NMR NOESY experiments, with distances from peak integration in good agreement with simulation distances. Further, in

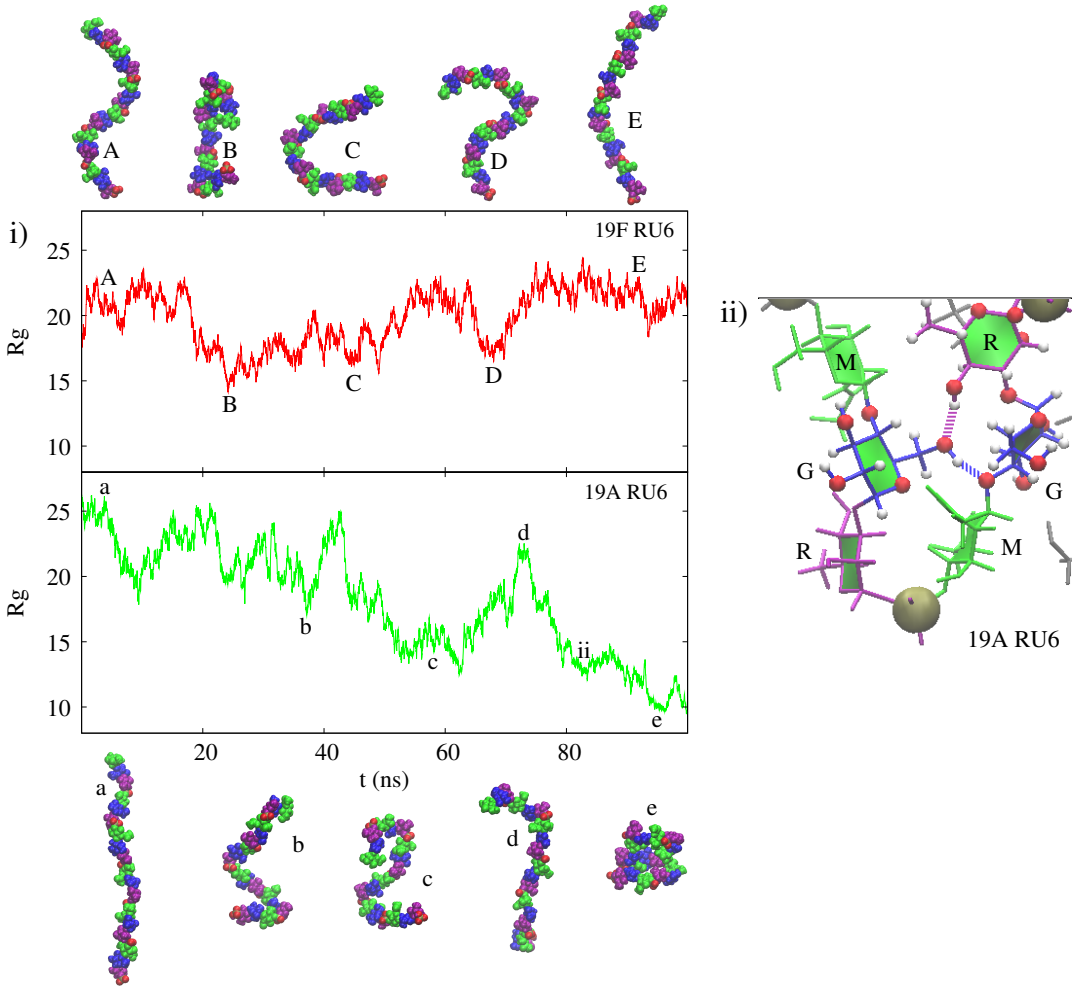
i)
A
B
C
D
E
19F RU6
Rg
25
20
15
10
A
B
C
D
E
19A RU6
a
b
c
d
e
ii
20
40
60
80
t (ns)
ii)
M
R
G
G
R
M
19A RU6

Figure 5:

our simulations, the 19F oligosaccharide adopts more extended conformations than 19A: tight hairpin bends around the phosphodiester linkage are favoured in 19A by the close stacking of successive repeating units allowed by the Glcα(1$\rightarrow$3)Rha linkage. These structural differences could account for the lack of cross-protection of serotype 19F vaccination against serotype 19A disease.

Therefore, we have shown that a slight difference in glycosidic linkage conformation can have a significant affect, not only the conformation of the repeating unit, but the polysaccharide as a whole. We are extending our systematic approach — analysis of the carbohydrate backbone from individual disaccharide pairs to 6RU chains — to the study of closely related bacterial capsular polysaccharide serotypes where similar structures of the capsular polysaccharide repeating unit also elicit distinct immune responses.

5. Acknowledgements

The South African Medical Research Council funding agency provided financial support for this work. Computations were performed using facilities provided by the University of Cape Town's ICTS High Performance Computing team: http://hpc.uct.ac.za. The authors thank PATH for the polysaccharide samples and A.D. MacKerell, Jr. for helpful email discussions.

[1] K. Elberse, S. Witteveen, H. van der Heide, I. van de Pol, C. Schot, A. van der Ende, G. Berbers, L. Schouls, Sequence diversity within the capsular genes of *streptococcus pneumoniae* serogroup 6 and 19, PLoS ONE 6 (9) (2011) e25018.

[2] H. Lee, M. H. Nahm, R. Burton, K. H. Kim, Immune response in infants to the heptavalent pneumococcal conjugate vaccine against vaccine-related serotypes 6a and 19a. clinical and vaccine immunology, Clin. Vaccine Immunol. 16 (3) (2009) 376–381.

[3] S. L. Kaplan, W. J. Barson, P. L. Lin, S. H. Stovall, J. S. Bradley, T. Q. Tan, J. A. Hoffman, L. B. Givne, E. O. Mason, Serotype 19a is the most common serotype causing invasive pneumococcal infections in children., Pediatrics 125 (3) (2010) 429–436.

[4] Center for Disease Control, Invasive pneumococcal disease in children 5 years after conjugate vaccine introduction - eight states, 1998-2005, MMWR 57 (6) (2008) 144–148.

[5] M. H. Nahm, J. V. Olander, M. Magyarlaki, Identification of cross-reactive antibodies with low opsonophagocytic activity for streptococcus pneumoniae., J. Infect. Dis. 176 (3) (1997) 698–703.

[6] C. E. Rose, S. Romero-Steiner, R. L. Carlone, D. Goldblatt, M. H. Nahm, L. Ashton, M. Haston, N. Ekstr *o*m, R. Haikala, H. Käyhty, I. Henckaerts, N. Durant, J. T. Poolman, P. Fernsten, X. Yu, B. T. Hu, K. U. Jansen, M. Blake, E. R. Simonetti, P. W. M. Hermans, B. D. Plikaytis, Multilaboratory comparison of streptococcus pneumoniae opsonophagocytic killing assays and their level of agreement for the determination of functional antibody activity in human reference sera., Clin. Vaccine Immunol. 18 (1) (2011) 135–142.

[7] W. R. Usinger, A. H. Lucas, Avidity as a determinant of the protective

efficacy of human antibodies to pneumococcal capsular polysaccharides., Infect. Immun. 67 (5) (1999) 2366–2370.

[8] R. L. Penn, E. B. Lewin, R. G. Douglas, G. Schiffman, C. J. Lee, J. B. Robbins, Antibody responses in adult volunteers to pneumococcal polysaccharide types 19f and 19a administered singly and in combination., Infect Immun 36 (3) (1982) 1261–1262.

[9] J. B. Robbins, R. Austrian, C. J. Lee, S. C. Rastogi, G. S. et al., Considerations for formulating the second-generation pneumococcal capsular polysaccharide vaccine with emphasis on the cross-reactive types within groups., J. Infect. Dis. 148 (5) (1983) 1136–1159.

[10] L. R. Grant, S. E. O'Brien, P. Burbidge, M. Haston, M. Zancolli, L. Cowell, M. Johnson, R. C. Weatherholtz, R. Reid, M. Santosham, K. L. O'Brien, D. Goldblatt, Comparative immunogenicity of 7 and 13-valent pneumococcal conjugate vaccines and the development of functional antibodies to cross-reactive serotypes., PLoS ONE 8 (9) (2013) e74906.

[11] N. J. Andrews, P. A. Waight, P. Burbidge, E. Pearce, L. Roalfe, M. Zancolli, M. Slack, S. N. Ladhani, E. Miller, D. Goldblatt., Serotype-specific effectiveness and correlates of protection for the 13-valent pneumococcal conjugate vaccine: a postlicensure indirect cohort study., Lancet Infect Dis 14 (9) (2014) 839–846.

[12] J. Poolman, C. Frasch, A. Nurkka, H. Käyhty, R. Biemans, L. Schuerman, Impact of the conjugation method on the immunogenicity of strep-

tococcus pneumoniae serotype 19F polysaccharide in conjugate vaccines, Clin. Vaccine Immunol. 18 (2) (2011) 327–336.

[13] W. P. Hausdorff, B. Hoet, R. A. Adegbola, Predicting the impact of new pneumococcal conjugate vaccines: serotype composition is not enough., Expert Rev. Vaccines (2014) 1–16.

[14] M. Kuttel, M. Gordon, N. Ravenscroft, Comparative simulation of pneumococcal serogroup 19 polysaccharide repeating units with two carbohydrate force fields., Carbohydr. Res. 390 (2014) 20–27.

[15] J. C. Phillips, R. Braun, W. Wang, J. Gumbart, E. Tajkhorshid, E. Villa, C. Chipot, R. D. Skeel, L. Kale, K. Schulten., Scalable molecular dynamics with namd, J. Comput. Chem. 26 (2005) 1781–1802.

[16] J. E. Stone, J. C. Phillips, P. L. Freddolino, . J. Hardy, L. G. Trabuco, K. Schulten, Accelerating molecular modeling applications with graphics processors, J. Comput. Chem. 28 (16) (2007) 2618–2639.

[17] W. L. Jorgensen, J. Chandrasekhar, J. D. Madura, R. W. Impey, M. L. Klein, Comparison of simple potential functions for simulations of liquid water., J. Chem. Phys 79 (2) (1983) 926–935.

[18] O. Guvench, S. N. Greene, G. Kamath, J. W. Brady, R. M. Venable, R. W. Pastor, A. D. MacKerell, Additive empirical force field for hexopyranose monosaccharides, J. Comput. Chem. 29 (15) (2008) 2543–2564.

[19] O. Guvench, E. Hatcher, R. M. Venable, R. W. Pastor, J. Alexander D. MacKerell, CHARMM additive all-atom force field for glycosidic

linkages between hexopyranoses, J. Chem. Theory Comput. 5 (9) (2009) 2353–2370.

[20] S. S. Mallajosyula, O. Guvench, E. Hatcher, A. D. MacKerell, Jr., CHARMM additive all-atom force field for phosphate and sulfate linked to carbohydrates., J. Chem. Theory Comput. 8 (2012) 759–776.

[21] A. D. MacKerell, Jr., Suggested approach for addition of phosphate linkages to charmm carbohydrate force field., personal communication (January 2014).

[22] M. Kuttel, N. Ravenscroft, M. Foschiatti, P. Cescutti, R. Rizzo, Conformational properties of two exopolysaccharides produced by inquilinus limosus, a cystic fibrosis lung pathogen, Carbohydr. Res. 350 (2012) 40–48.

[23] J. E. Stone, VMD psfgen plugin [cited 12 November 2014].
URL `http://www.ks.uiuc.edu/Research/vmd/plugins/psfgen/`

[24] W. Humphrey, A. Dalke, K. Schulten, VMD – Visual Molecular Dynamics, J. Molec. Graphics 14 (1996) 33–38.

[25] S. E. Feller, Y. Zhang, R. W. Pastor, B. R. Brooks, Constant pressure molecular dynamics simulation: The langevin piston method, J.Chem. Phys. 103 (11) (1995) 4613–4621.

[26] S. Nose, M. L. Lein, Constant pressure molecular dynamics for molecular systems., Mol. Phys. 50 (1983) 1055–1076.

[27] W. G. Hoover, Canonical dynamics: Equilibrium phase-space distributions, Phys. Rev. A 31 (1985) 1965–1697.

[28] M. Kuttel, J. Gain, A. Burger, I. Eborn, Techniques for visualization of carbohydrate molecules, J. Mol. Graphics Modell. 25 (2006) 380–388.

[29] L. J. Heyer, S. Kruglyak, S. Yooseph, Exploring expression data: Identification and analysis of coexpressed genes, Genome Res. 9 (1999) 1106–1115.

[30] H. J. Jennings, K. G. Rosell, D. J. Carlo, Structural determination of the capsular polysaccharide of streptococcus pneumoniae type-19 (19F)., Can. J. Chem 58 (11) (1980) 1069–1074.

[31] E. Katzenellenbogen, H. J. Jennings, Structural determination of the capsular polysaccharide of *streptococcus pneumoniae* type 19A., Carbohydr. Res. 124 (2) (1983) 235–245.

[32] P. D. Thomas, V. J. Basus, T. L. James, Protein solution structure determination from two-dimensional nuclear overhauser effect experiments: Effect of approximations on the accuracy of derived structures, Proc. Natl. Acad. Sci. U.S.A. 88 (1991) 1237–1241.

Figure and Table Captions

Table 1. Inter-atomic distances (Å) for 19F and 19A from NMR and simulation.

Figure 1. Plots for 19F (left, red) and 19A (right, green) of the M14G and G12R/G13R ϕ,ψ simulation time series superimposed on the corresponding disaccharide vacuum free energy surfaces[14] for RU1 (top, prior work[14]), RU3 (middle) and RU6 (bottom). The first 10 ns of simulation were discarded as equilibration. RU3 shows time series for the middle repeating unit only (highlighted in the structures); RU6 the time series for repeating units 3 and 4 (also highlighted in the corresponding structures). Structures are annotated to indicate residue identity: ManNAc (M, green), Glc (G, blue) and Rha (R, purple).

Figure 2. Time series of the H1 Glc/H1 Rha and H1 Glc/H3 Rha distances for the middle repeat unit in the RU3 simulations of 19F (red, top and left) and 19A (green, bottom and right). Distances from NMR are indicated by dashed lines. Representative conformations for the middle RU are shown for 19F (left) and 19A (right), with key atoms and distances indicated. Structures are annotated to indicate residue identity: ManNAc (M, green), Glc (G, blue) and Rha (R, purple).

Figure 3. Selected regions of the 2D ^{1}H-^{1}H-NOESY spectra of polysaccharide serotype 19F (A) and 19A (B) recorded at ^{1}H frequency of 600

MHz and with a mixing time of 250 ms. Key correlations from the anomeric protons are annotated.

Figure 4. Comparison of the hydrodynamic behaviour of the RU3 19F and 19A polysaccharides. i) Time series of the instantaneous values of the radius of gyration (Å) for the RU3 simulations of the 19F (red line, top) and 19A (green line, bottom) polysaccharides. Representative structures are shown (19F top and 19A bottom) and the average radius of gyration indicated dashed lines. ii) Snapshot at 84 ns of a hairpin bend in 19A RU3, showing stabilizing hydrogen bonding interactions (dashed lines) between adjacent repeat units. iii) Time autocorrelation function for the radius of gyration for the RU3 simulations in 19F (red line) and 19A (green line).

Figure 5. Comparison of the hydrodynamic behaviour of the RU6 19F and 19A polysaccharides. i) Time series of the instantaneous values of the radius of gyration (Å) for the RU6 simulations of the 19F (red line, top) and 19A (green line, bottom) polysaccharides. Representative structures are shown (19F top and 19A bottom). ii) Closeup at 84 ns of a hairpin bend in 19A, showing stabilizing hydrogen bonding interactions (dashed lines) between adjacent repeat units.